MDPI

Article

Fluid–Structure Interaction and Non-Fourier Effects in Coupled Electro-Thermo-Mechanical Models for Cardiac Ablation

Sundeep Singh [1,2,*] and **Roderick Melnik** [2,3]

1 Schulich School of Engineering, University of Calgary, 2500 University Drive NW, Calgary, AB T2N 1N4, Canada
2 MS2Discovery Interdisciplinary Research Institute, Wilfrid Laurier University, 75 University Avenue West, Waterloo, ON N2L 3C5, Canada; rmelnik@wlu.ca
3 BCAM—Basque Center for Applied Mathematics, Alameda de Mazarredo 14, E-48009 Bilbao, Spain
* Correspondence: ssingh@wlu.ca

Abstract: In this study, a fully coupled electro-thermo-mechanical model of radiofrequency (RF)-assisted cardiac ablation has been developed, incorporating fluid–structure interaction, thermal relaxation time effects and porous media approach. A non-Fourier based bio-heat transfer model has been used for predicting the temperature distribution and ablation zone during the cardiac ablation. The blood has been modeled as a Newtonian fluid and the velocity fields are obtained utilizing the Navier–Stokes equations. The thermal stresses induced due to the heating of the cardiac tissue have also been accounted. Parametric studies have been conducted to investigate the effect of cardiac tissue porosity, thermal relaxation time effects, electrode insertion depths and orientations on the treatment outcomes of the cardiac ablation. The results are presented in terms of predicted temperature distributions and ablation volumes for different cases of interest utilizing a finite element based COMSOL Multiphysics software. It has been found that electrode insertion depth and orientation has a significant effect on the treatment outcomes of cardiac ablation. Further, porosity of cardiac tissue also plays an important role in the prediction of temperature distribution and ablation volume during RF-assisted cardiac ablation. Moreover, thermal relaxation times only affect the treatment outcomes for shorter treatment times of less than 30 s.

Keywords: cardiac ablation; fluid–structure interaction; porous media; relaxation time effects; bio-heat transfer; numerical simulations

1. Introduction

Minimally invasive thermal therapies are nowadays recognized as the fourth pillar of interventional oncology. In the past two decades, the feasibility and efficacy of thermal ablative procedures (viz., radiofrequency (RF), laser, microwave, cryo- and ultrasound ablations) have been widely explored and reported for treating different types of cancer [1–3]. Apart from providing curative and palliative treatment to vast varieties of benign and malignant tumors, these therapies have also been explored as a promising alternative treatment modalities for treating cardiovascular diseases, neurodegenerative disorders and chronic pain [4,5]. Over the past two decades, numerical modeling and simulations have played a vital role in providing a better understanding of complex biophysical phenomena and the effects of associated intrinsic and extrinsic factors on the efficacy of thermal ablative procedures. They also provide a quick, safe, cheap and viable alternative for predicting a priori information about the treatment outcomes of the thermal ablative procedures that could play an important role in the treatment planning stage of thermal therapies.

Several numerical studies have been reported in the past on the modeling of the RF-assisted cardiac ablation [6–10]. Most of these studies are based on the coupled electro-thermal problem whereby the Fourier's law based Pennes bioheat transfer equation is coupled with the quasi-static electric potential equation to obtain the induced temperature

distribution and the ablation volume. The cooling (heat-sink) effect caused by the blood flow within the cardiac chamber is often described by the convective boundary conditions. Due to its simplicity, Pennes equation is the widely used bioheat transfer model for modeling the heat transport in cardiac tissue during RF-assisted ablation. However, Pennes bioheat transfer model relies on several assumptions, viz., considers a uniform perfusion rate, neglects blood flow direction and the artery-vein countercurrent arrangement, and considers arterial blood temperature to be constant at 37 °C [11]. To address this issue, porous media approach has been utilized which is based on fewer assumptions as compared to Pennes equation and thus provides a better prediction of the temperature distribution during thermal ablative procedures [4,11,12]. Numerical studies have also been reported to incorporate the mechanical deviations induced due to insertion of the electrode in the myocardium tissue during RF ablation [13–16]. Recently, comparative analysis has also been conducted to quantify the differences in applied electrical power between full thorax models and limited-domain models for RF-assisted cardiac ablation [17,18]. A brief recent survey of coupled thermo-electro-mechanical models of cardiac ablation from a multiscale perspective can be found in [19]. Thus, significant efforts have been made in the past to refine the numerical models of cardiac ablation and to mitigate the deviations obtained in the numerical and experimental predications. Moving further in this direction, we report a fully coupled electro-thermo-mechanical model to provide more realistic and accurate predictions of the treatment outcomes during the RF-assisted cardiac ablation. The developed model accounts for the non-Fourier thermal relaxation time effects, fluid–structure interactions and porous media approach. Parametric studies have been conducted to systematically investigate the effect of porosity, thermal relaxation times, blood flow velocity, electrode insertion depth and electrode orientation on the treatment outcomes of RF-assisted cardiac ablative procedures.

2. Materials and Methods

Figure 1 presents the schematic of three-dimensional computational domain considered in the present numerical study for simulating the RF-assisted cardiac ablation. In particular, the considered model comprises of a fragment of cardiac tissue, blood chamber and an open-irrigated electrode (7 Fr diameter and 4 mm length) [8,10]. Replicating actual clinical scenarios, a force is applied at the top of the electrode, resulting in its insertion within the cardiac tissue to a depth of up to 2 mm, which has proved to be safer and effective in clinical studies reported in the literature [15]. The material properties for the different domains considered in this study are presented in Table 1 [8,10,13–16,20–22].

Table 1. Material properties considered in the present study for different domains.

Parameter	Myocardium/ Cardiac Tissue	Blood/ Cardiac Chamber	Electrode (Active Part)	Catheter (Insulated Part)
Density ρ (kg/m^3)	1060	1000	21,500	70
Specific heat c (J/(kg·K))	3111	4180	132	1045
Thermal conductivity k (W/(m·K))	0.53	0.541	71	0.026
Electrical conductivity σ (S/m)	0.54	0.667	4.6×10^6	10^{-5}
Thermal expansion coefficient α (K^{-1})	1×10^{-4}	–	–	–
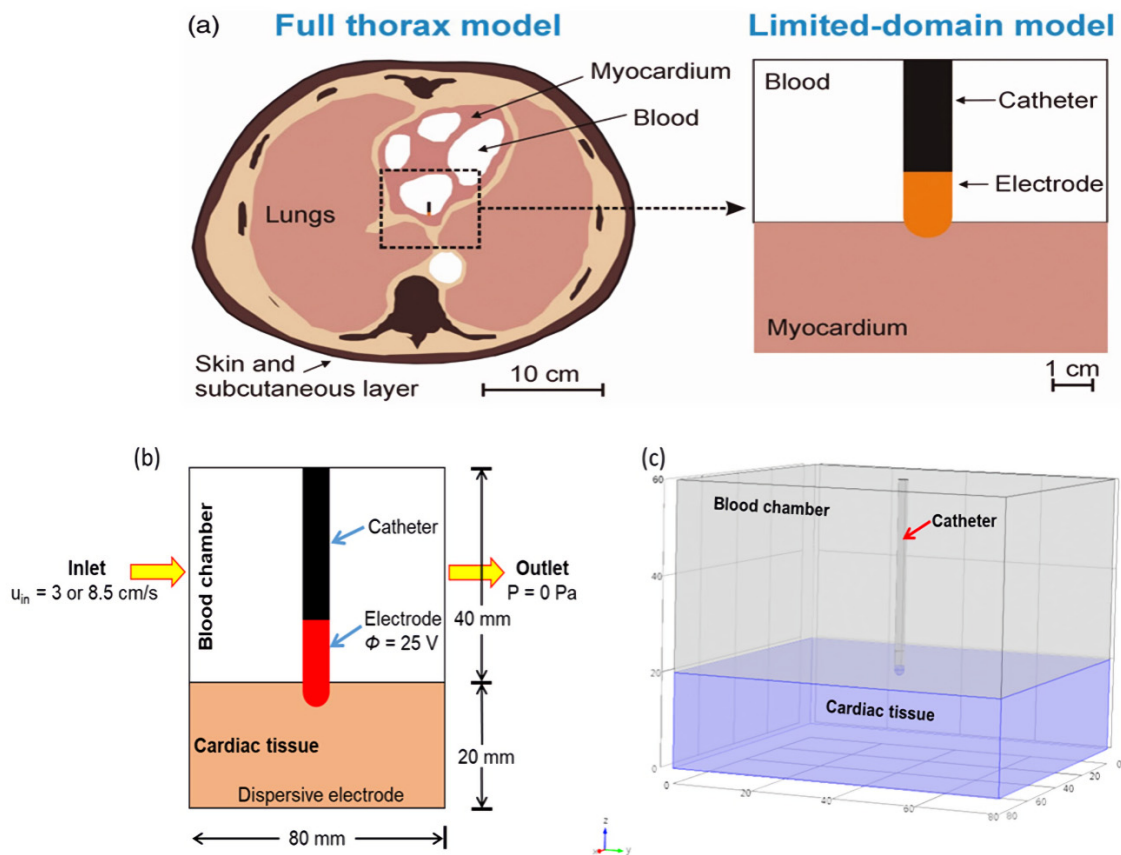
Figure 1. (**a**) Reduction of computational domain from full thorax model to limited domain model (reproduced from Irastorza et al. [17] under the terms of the Creative Commons CC BY license for an open access article). (**b**) Boundary conditions associated with the limited-domain model considered in the present numerical study. (**c**) Schematic of three-dimensional model derived from the selected control volume of limited-domain model.

The transient temperature distribution and ablation volume attained within the porous myocardium tissue during RF-assisted cardiac ablation have been computed utilizing the coupled electro-thermo-mechanical model incorporating non-Fourier effects and fluid–structure interactions. Further, in this numerical study the porous media based local thermal equilibrium (LTE) formulation has been used to compute the temperature distribution during cardiac ablation that assumes tissue phase temperature to be equal to fluid phase temperature everywhere within the porous tissue [23]. The non-Fourier based bioheat transfer equation for porous medium incorporating two phase lags (τ_q and τ_t) can be represented as [4,24].

$$(\rho c)_{eff} \frac{\partial T}{\partial t} + (\rho c)_b \vec{\mathrm{u}} \cdot \nabla T = k_{eff} \left[\nabla^2 T + \tau_t \frac{\partial}{\partial t} \left(\nabla^2 T \right) \right] + Q_p, \tag{1}$$

where τ_q is the thermal relaxation time that represents the time delay between heat flux and the associated heat conduction through a medium (i.e., the delay arising from thermal inertia) [21,25], τ_t is the phase lag in establishing temperature gradient across the medium (i.e., the delay arising from micro-structural interactions). While the models accounting for thermal relaxation in the context of hyperbolic thermo-elasticity have a longer history [26–28], a comprehensive analysis and applications of such models in the context of thermal ablation of biological tissues are fairly new [21]. Due to two associated phase lags, Equation (1) is often referred to as a dual phase lag (DPL) model that will be reduced to single phase lag (SPL) for $\tau_q \neq 0$, $\tau_t = 0$, and Fourier's law based Pennes bioheat transfer equation for $\tau_q = \tau_t = 0$. ρ is the density, c is the specific heat capacity, k is the thermal conductivity, $\vec{\mathrm{u}}$ is the velocity vector. T is the temperature to be computed during

RF-assisted cardiac ablation. Q_p is the resistive heat generated due to RF heating and under quasi-static approximation of Maxwell's equation, it is represented as the product of current density (J) and electric filed intensity (E), i.e., $Q_p = J \cdot E = \sigma E^2$ (W/m^3), where σ is the electrical conductivity of the biological tissue. The effective heat capacity and the thermal conductivity of porous cardiac tissue are given by:

$$
\begin{aligned}
(\rho c)_{eff} &= \varepsilon \rho_t c_t + (1 - \varepsilon)\rho_b c_b, \\
k_{eff} &= \varepsilon k_t + (1 - \varepsilon)k_b,
\end{aligned}
\tag{2}
$$

where ε is the porosity of the tissue, i.e., the ratio of blood volume to the total volume. Subscripts *eff*, *t* and *b* stand for effective, tissue and blood, respectively. Motivated by [8,14], both electrical and thermal conductivities have been modeled as temperature dependent properties. The blood flow within the porous domain has been modeled assuming the laminar, incompressible, Newtonian flow as given by the modified Navier–Stokes equation [20,29], as follows:

$$
\begin{aligned}
\nabla \vec{u} &= 0, \\
\rho_b \left(\frac{\partial \vec{u}}{\partial t} + \vec{u} \cdot \nabla \vec{u} \right) &= -\nabla P + \frac{\mu}{\varepsilon} \nabla^2 \vec{u} - \frac{\mu}{K} \vec{u},
\end{aligned}
\tag{3}
$$

where $\vec{u}(= u_x, u_y, u_z)$ is the velocity vector, ρ_b is the density of blood, P is the blood pressure, μ is the dynamic viscosity of blood (= 2.1×10^{-3} Pa·s), ε is the porosity and K is the permeability of porous cardiac tissue (= 7.7×10^{-11} m^2). Other models for the fluid part of the fluid–structure interaction (FSI) problem can be easily incorporated in the proposed framework, including those based on non-Newtonian flows (e.g., [30–34]). Although not yet fully integrated with the models for ablation therapies, the cardiac fluid dynamics models have been an area of active research from theoretical, numerical, and experimental perspectives [35–37]. Likewise, FSI problems have received significant attention of the research community [38–46]. In our present context, it should be noted that while the research in cardiovascular modeling also covers cardiac electro-mechanical coupling, specifics of ablation problems require new models and new approaches for their solution.

The thermo-elastic deformation caused by non-uniform heating during cardiac ablation has been quantified using the modified stress–strain equation incorporating thermal expansion effects [4,14], as:

$$
\overline{\sigma}_{ij} = 2\overline{\mu}\varepsilon_{ij} + \lambda \varepsilon_{kk}\delta_{ij} - (3\lambda + 2\overline{\mu})\varepsilon^{th}\delta_{ij},
\tag{4}
$$

where $\overline{\sigma}$ is the stress tensor, $\overline{\mu} = [\overline{E}/2(1 + v)]$ and $\lambda = [v\overline{E}/(1 + v)(1 - 2v)]$ are the Lame's constants, $\overline{E}$ is the Young's modulus, v is the Poisson's ratio, $\varepsilon = [(\nabla \overline{u}^T + \nabla \overline{u})/2]$ is the strain tensor, $\overline{u}$ is the mechanical displacement vector, $\varepsilon^{th} = \left(\int_{T_{ref}}^{T} \alpha \, dT \right)$ is the thermal strain, α is the thermal expansion coefficient, T is the temperature computed from bio-heat transfer model, $T_{ref} = 37$ °C is the reference temperature and δ is the Kronecker delta function given by:

$$
\delta_{ij} = \begin{cases} 1 & for\ i = j \\ 0 & for\ i \neq j \end{cases}.
\tag{5}
$$

The general form of the thermo-elastic wave equation for the non-rigid mechanics can be expressed as [4,14]:

$$
\rho \frac{\partial^2 u}{\partial t^2} = \overline{\sigma}_{ij,j} + F_i,
\tag{6}
$$

where ρ is the density of the material, $\overline{\sigma}$ is the stress tensor given by Equation (4) ($i, j = 1, 2, 3$ are the tensor indices representing geometry's coordinate axes), $\overline{u}$ is the mechanical displacement vector, t is the time and F is the external body force. The myocardium tissue

has been modeled as a linearly elastic, isotropic and homogeneous material with $\overline{E}$ = 75 kPa and v = 0.49, while the Young's modulus of elasticity and Poisson's ratio of the RF electrode has been considered to be 168 GPa and 0.38, respectively [13,21].

A 60 s cardiac ablation procedure has been modeled by applying a Dirichlet voltage boundary condition (=25 V) at the active tip of the electrode [6]. At the bottom surface of the computational domain 0 V electric potential has been applied to model the dispersive (ground) electrode. The initial voltage and the initial temperature of the entire computational domain have been set to 0 V and 37 °C, respectively. At each interface within the computational domain, electrical, thermal and mechanical continuity boundary conditions have been imposed. The saline flow from the holes of an open-irrigated electrode has been modeled by specifying a 45 °C constant temperature at the active electrode surface not inserted within the cardiac tissue [8,10]. Notably, the induced ablation volume during the RF-assisted cardiac ablation has been quantified utilizing the 50 °C isotherm contour, which represents the volume of myocardium tissue having a temperature ≥50 °C after the selected treatment time [6–8,10,13–16]. A finite-element method (FEM) based COMSOL Multiphysics 5.2 software [47] has been used to solve the coupled electro-thermo-mechanical problem for computing electric field and temperature distributions, ablation volumes and thermally induced stresses within the cardiac tissue post cardiac ablative procedures. The computational domain has been discretized using the heterogeneous tetrahedral mesh elements with further refinements close to the active tip of the electrode where higher electrical, thermal and mechanical gradients are expected. Mesh sensitivity studies have been conducted to compute the optimal number of mesh elements by progressively refining the mesh until the absolute error for maximum temperature is less than 0.5% compared to the previous mesh size. The final mesh consists of 83324 elements. All FEM simulations presented in the next section have been conducted on the 64-bit 10 core Intel® Xeon® E5-2680 v2 @ 2.80 GHz processor.

3. Results and Discussion

In this section, we will present the results derived from the developed fully coupled electro-thermo-mechanical models of the cardiac ablation incorporating: (a) fluid–structure interaction, (b) non-Fourier based heat transfer, and (c) a porous media approach. In what follows, we provide details of a systematic analysis of the effects of porosity, thermal relaxation times (both single and dual phase lags), blood flow velocity, electrode insertion depth and electrode orientation on the temperature distribution and ablation volume.

The fidelity and integrity of the developed model have been evaluated by comparing the results obtained from the present model with those available in the literature, in particular [6], incorporating similar geometrical configurations, thermo-physical properties, initial and boundary conditions. The comparative analysis of the outcomes of the model with that of [6] is presented in Table 2 for both low and high blood flow conditions considered in the present numerical study. As evident from Table 2, the predicted results of the developed model are in good agreement with those reported in [6] after 60 s of RF-assisted cardiac ablation utilizing constant voltage of 25 V, and as such the model has been validated and lends great confidence in the reported results discussed next.

Table 2. Validation of the predicted results of current model with that of [6].

Parameter	Low Blood Flow u = 3 cm/s		High Blood Flow u = 8.5 cm/s	
	Previous Study [6]	Present FEM Study	Previous Study [6]	Present FEM Study
Depth of lesion	7.64 mm	7.62 mm	7.53 mm	7.53 mm
Maximum width of lesion	12.81 mm	12.80 mm	11.92 mm	11.90 mm
Maximum temperature in the tissue	111.3 °C	110.8 °C	102.4 °C	101.9 °C
Maximum temperature in the blood	89.6 °C	89.2 °C	79.9 °C	79.7 °C

3.1. Coupled Electro-Thermo-Mechanical Model of Cardiac Ablation

Figure 2 presents the induced temperature, von Mises stress and volumetric strain distributions predicted after 15, 30 and 60 s of the cardiac ablation procedure with a porosity of 0.3, blood flow of u_{in} = 3 cm/s, thermal lags of τ_q = 8 s, τ_t = 0.045 s, insertion depth of 2 mm and perpendicular orientation of electrode. As evident from Figure 2a–c, the temperature distribution within the cardiac tissue is of the ellipsoid shape which is consistent with the other modeling studies available in the literature. Further, due to the blood flow in the cardiac chamber (from left to right face), the temperature distribution is not symmetric along the electrode insertion axis. Rather, the temperature distribution in the downstream of the electrode is slightly higher as compared to the upstream side. This can be attributed to the fact that at the upstream side the RF electrode obstructs the path of the blood flow within the blood chamber and accordingly the blood velocity will be slightly higher at upstream side as compared to downstream side of the electrode. This could eventually lead to an enhanced heat-sink effect whereby the heat generated due to the high-frequency RF currents is being carried away by the flowing blood.
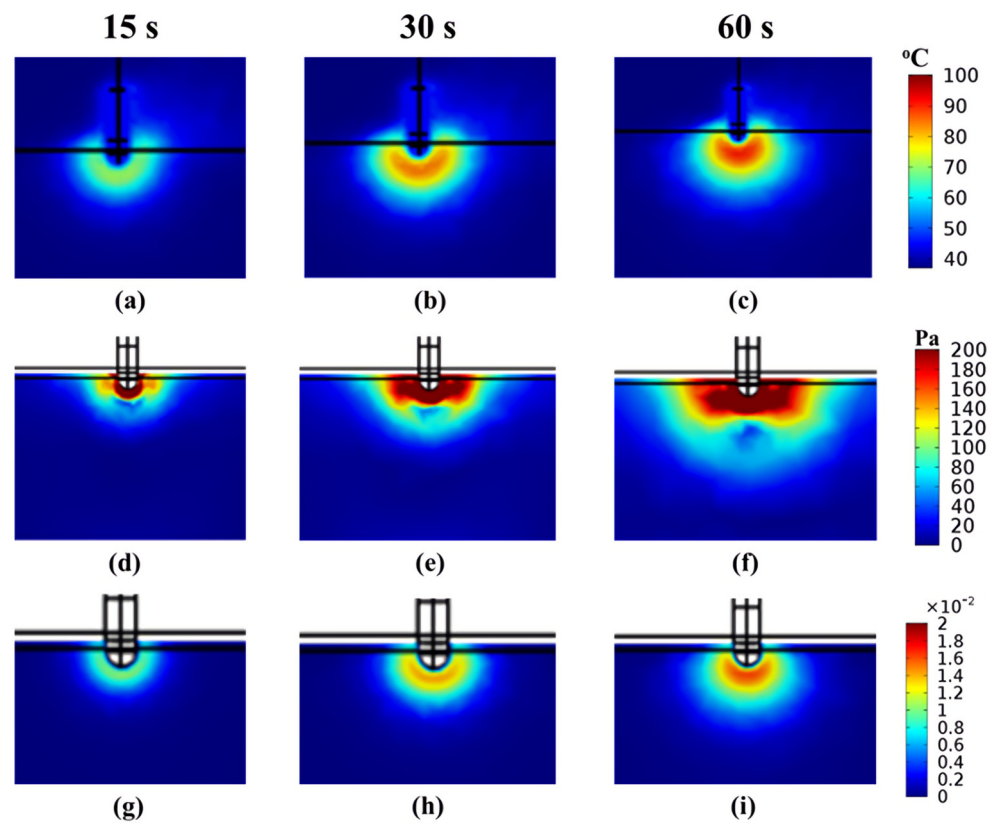

Figure 2. Temporal evolution of: (**a**–**c**) temperature, (**d**–**f**) von Mises stress, and (**g**–**i**) volumetric strain distributions during cardiac ablation procedure.

Moreover, the hot spot zone during the 60 s of cardiac ablation procedure is induced just beneath the tip of the RF electrode within the cardiac tissue. Alongside the cardiac tissue, a significant portion of the blood in the cardiac chamber (mainly close to the electrode surface) is also exposed to elevated temperature greater than 50 °C. Thus, the present study not only allows the accurate prediction of the cardiac tissue temperature, but also provides the accurate estimate of the blood temperature during the cardiac ablation procedure. Further, as mentioned earlier, the higher thermal stresses induced within the cardiac tissue during the RF procedure could also result in the nociception of the thermal pain. The von Mises stresses obtained from the coupled electro-thermo-mechanical model have been presented in Figure 2d–f. Notably, in continuum mechanics von Mises stress provides an indication of whether the induced stress will lead to material failure or not.

Figure 2g–i presents the volumetric strain induced within the cardiac tissue. As evident, the portion of the cardiac tissue that was exposed to the higher temperature experiences higher volumetric strain.

3.2. Effect of Porosity

In this study, porous media theory has been used for modeling the heat transport within the cardiac tissue during RF assisted cardiac ablation. Notably, LTE formulation has been used, which assumes the temperature of the tissue phase locally equal to the blood phase within the porous medium. Moreover, the porosity of the biological tissue is likely to change during the minimally invasive thermal ablative procedure owing to the natural body temperature regulation system that controls the body temperature by regulating blood flow within the porous biological structure [23]. This regulation system could increase or decrease the porosity of the biological medium, and hence effective thermal conductivity of the porous medium, based on the temperature changes induced within the tissue during thermal ablation. Thus, we have quantified the effect of changes in porosity on the tissue and blood temperature distributions, and the attained ablation volume during the cardiac ablation procedure. Motivated by [11,20,48], three values of porosity have been selected for the biological tissue, viz., ε = 0.05, 0.3, 0.6. Importantly, in the present study the ablation volume refers to the volume of cardiac tissue having a temperature greater than or equal to 50 °C [14,49–52]. Figure 3a presents the temporal variation of temperature at a point 1 mm away from the tip of the electrode along the line of electrode insertion for different values of porosity of cardiac tissue. As evident from this figure, the changes in porosity do not affect the predicted temperature profile approximately till first 30 s of the RF assisted cardiac ablation. Beyond that there prevails a significant variation in the temperature profile for considered values of porosity. The increase in porosity from 0.05 to 0.6 decreases the magnitude of temperature by 5.37 °C after 60 s of cardiac ablation. The effect of variation in cardiac tissue porosity on the maximum tissue and blood temperatures have been presented in Figure 3b,c, respectively. Again, the variation of the maximum tissue temperature for different values of porosity is negligible up to first 30 s of cardiac ablation and it eventually increases thereafter. The change in porosity from 0.05 to 0.6 results in a decline of 6.86% in the predicted value of the maximum temperature attained within the tissue after 60 s of cardiac ablation. The varying cardiac porosity has very negligible influence on the maximum blood temperature, as evident from Figure 3c. Moreover, as seen from Figure 3a–c the temperature distributions in both tissue and blood increase with an increase in heating time during the cardiac ablative procedure. Initially, the increase in temperature is asymptotic, which later stabilizes with the passage of time. Further, both tissue and blood temperature distributions follow similar trends, however the rise in blood temperature is significantly less than the tissue temperature due to the different RF powers absorbed within the tissue and blood during the cardiac ablation. Figure 3d presents the temporal variation of ablation volume attained during the 60 s cardiac ablation procedure. As evident, the ablation volume predicted with ε = 0.6 is significantly higher as compared to ε = 0.05. This can be attributed to the fact that the higher porosity of the cardiac tissue will result in higher volumetric transfer area between the blood and the tissue, resulting in higher ablation volume during the cardiac ablation. Thus, the variation in the porosity significantly affects the predicted outcomes of the cardiac ablation and must be accounted for obtaining accurate, precise and realistic predictions of tissue and blood temperatures as well as the attained ablation zone.
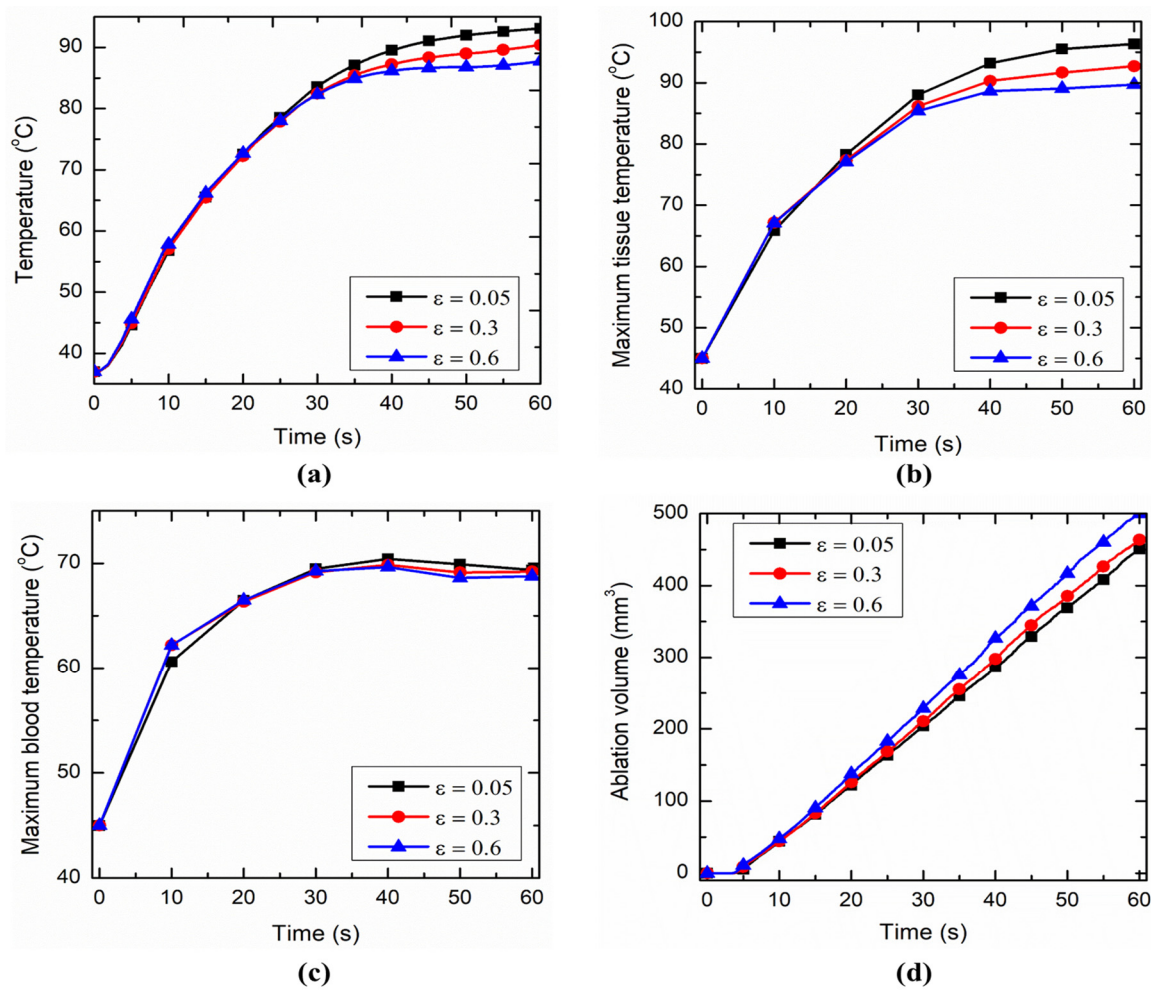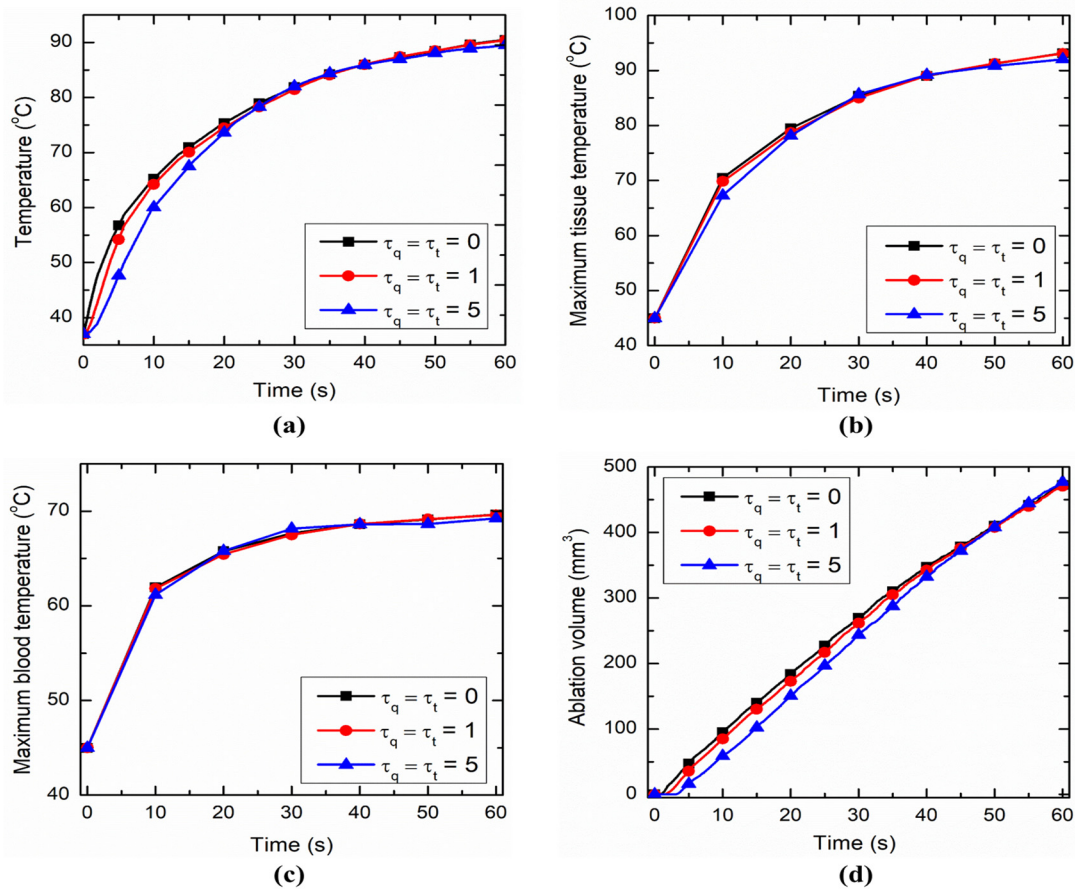
Figure 3. Temporal variation of: (**a**) temperature at a point 1 mm away from tip of electrode, (**b**) maximum tissue temperature, (**c**) maximum blood temperature, and (**d**) ablation volume for different values of porosity.

3.3. Effect of Thermal Relaxation Times

The heat transfer within the biological tissue has been modeled utilizing a dual-phase lag bio-heat transfer model considering two phase lags, τ_q and τ_t. Importantly, τ_q refers to the phase lag due to heat flux, i.e., time delay between the heat flux and the temperature variation. By virtue of this lag, the thermal energy propagation within the cardiac tissue during RF ablation is arrested. A higher value of τ_q results in higher energy accumulation within the biological tissue and consequently significantly higher vibration characteristics in response to the elevated temperatures; while τ_t refers to the phase lag due to the temperature gradient, i.e., heat flux vector precedes the temperature gradient. This lag eventually results in lower energy accumulation and lower peak temperatures within the biological tissue, and accordingly the increase in τ_t results in diminishing vibration characteristic in thermal response [53,54]. Motivated by [21,53,54], three values of thermal lag have been selected for the biological tissue, viz., $\tau_q = \tau_t = 0$ (Fourier model), 1, 5. The effect of thermal relaxation times (τ_q and τ_t) on the temperature distribution and ablation volume for cardiac ablation procedure has been presented in Figure 4 for $\varepsilon = 0.3$ and $u_{in} = 3$ cm/s. Figure 4a presents the temporal variation of temperature at a point 1 mm away from the RF electrode tip along the insertion axis for different values of thermal relaxation times.
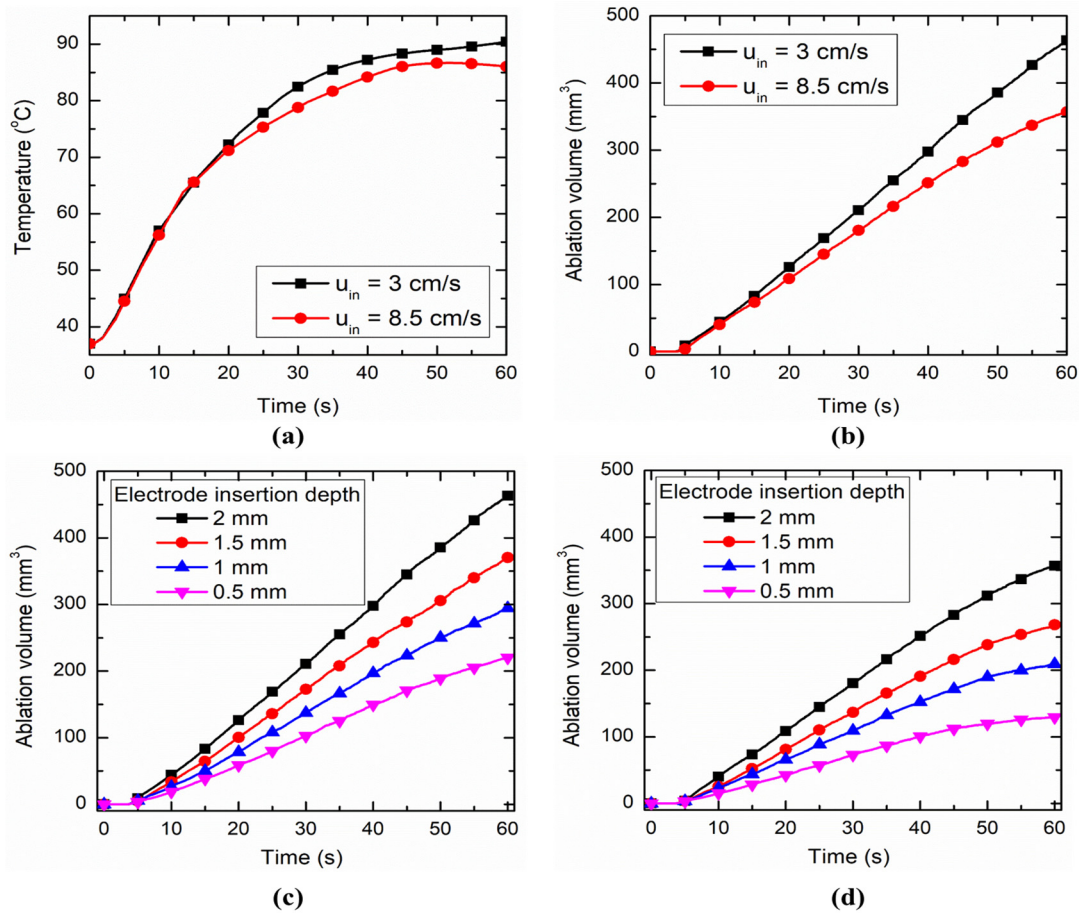
Figure 4. Temporal variation of: (**a**) temperature at a point 1 mm away from tip of electrode, (**b**) maximum tissue temperature, (**c**) maximum blood temperature, and (**d**) ablation volume for different values of thermal relaxation times.

As inferred from Figure 4a, there prevails significant deviations among the predicted values of the temperature for first 30 s of the cardiac ablation for different values of τ_q and τ_t. Eventually, beyond 30 s of ablation, the deviation between the predicted temperature for different values of thermal relaxation time diminishes with the passage of time. Similar variations have been seen in the ablation volume profile presented in Figure 4d. Moreover, the non-Fourier characteristics have a negligible effect on the maximum tissue and blood temperatures during the 60 s long cardiac ablation, as depicted in Figure 4b,c, respectively. Thus, for shorter duration of cardiac ablation, less than 30 s or so, the thermal relaxation times could significantly affect the predicted ablation volume, while for treatment times greater than 30 s, ablation volume is not sensitive to the value of thermal relaxation times.

3.4. Effect of Blood Flow in the FSI Problem and Electrode Insertion Depth

The effects of blood flow rate on the temperature distribution and ablation volume during cardiac ablation procedure have been presented in Figure 5a,b, respectively. Two blood flow conditions have been considered, viz., low blood flow rate (u_{in} = 3 cm/s) and high blood flow rate (u_{in} = 8.5 cm/s). As evident from Figure 5a,b, the temperature distribution and ablation volume profiles for low blood flow rate conditions are always on a higher side when compared to the high blood flow rate conditions, except for first 10 to 15 s of cardiac ablation, whereby the deviations among low and high blood flow rate conditions are quite negligible.

Figure 5. Temporal variation of: (**a**) temperature at a point 1 mm away from tip of electrode, and (**b**) ablation volume for different values of blood flow rates. (**c**) Comparison of ablation volumes predicted with different insertion depth of the electrodes for low blood flow rate and (**d**) high blood flow rate conditions.

The reduction in ablation volume size for high blood flow rate condition as compared to low blood flow rate can be attributed to the higher heat-sink affect induced by the high blood flow rate, thus carrying away the considerable portion of heat that was supposed to be deposited within the cardiac tissue during thermal ablative procedure and thus reducing the ablation zone. At the end of 60 s of cardiac ablation, the ablation volume attained with high blood flow rate condition is found to be 23.07% lower as compared to that obtained with low blood flow rate condition. Furthermore, the influence of electrode insertion depth on the ablation volume attained during the RF assisted cardiac ablation procedure has been presented in Figure 5c,d for both low and high blood flow rates conditions, respectively. As evident from these figures, for both cases the ablation volume abruptly increases with the increase in the insertion depth. This can be attributed to the fact that the larger the insertion depth of the RF electrode is, the more will be the contact surface of the electrode with the target tissue and lower the heat-sink effect caused by the flowing blood in the cardiac chamber, eventually resulting in enhanced delivery of the RF energy to the cardiac tissue and thus leading to significantly higher ablation volumes. It has been found that for the low blood flow rates, ablation volume increases by 33.79%, 68.22% and 110.53% for insertion depth of 1, 1.5 and 2 mm, respectively, as compared to the ablation volume quantified with 0.5 mm insertion depth of the electrode. Similarly, for the high blood flow rates condition, increase in ablation volume is 61.40%, 106.96% and 175.49% for electrode insertion depth of 1, 1.5, and 2 mm, respectively, as compared to 0.5 mm electrode insertion depth.

3.5. Effect of of Electrode Orientation

Apart from the RF electrode insertion depth, we have also numerically investigated the effects of RF electrode orientation on the treatment outcomes of cardiac ablative procedures. Motivated by [55], three RF electrode to tissue orientations have been considered, viz., perpendicular (90°), oblique (45°) and parallel (0°), as depicted in Figure 6a. The temperature distributions obtained for these three orientations have been presented in Figure 6b–d considering $\varepsilon = 0.3$ and $u_{in} = 3$ cm/s. As evident from this figure, the maximal depth of the lesion obtained after 60 s of cardiac ablation is nearly same for all orientations, while the maximal width of the lesion increases by decreasing the RF electrode orientation w.r.t tissue from 90° to 0°. This can be attributed to the fact that as the electrode orientation is decreased the contact surface area between the electrode tip and the cardiac tissue increases leading to enhanced delivery and accumulation of the RF energy within the tissue, thereby increasing the ablation zone attained after 60 s of the RF assisted cardiac ablation. The propagation of ablation volume after 15 s, 30 s and 60 s of cardiac ablation procedure has been presented in Figure 7 for different orientations of the electrode considered in the present study. Furthermore, the effects of electrode orientation on the maximum temperature distribution attained within the tissue and blood during 60 s of cardiac ablation have been presented in Figure 8a,b, respectively. As evident from these figures, the effect of electrode orientation is far more pronounced on the maximal blood temperature as compared to the tissue temperature. The maximal temperature profile is higher for the oblique orientation and lower for the parallel orientation of the RF electrode. Moreover, the temporal variations of the ablation volume for different orientations of the electrode have been presented in Figure 8c,d for low and high blood flow rates, respectively. The ablation volumes attained after 60 s of the RF assisted cardiac ablation for oblique and parallel orientations have been found to be 16.59% and 54.72% higher for low blood flow condition, respectively, and 17.92% and 63.73% for high blood flow condition, respectively, when compared to the perpendicular orientation.
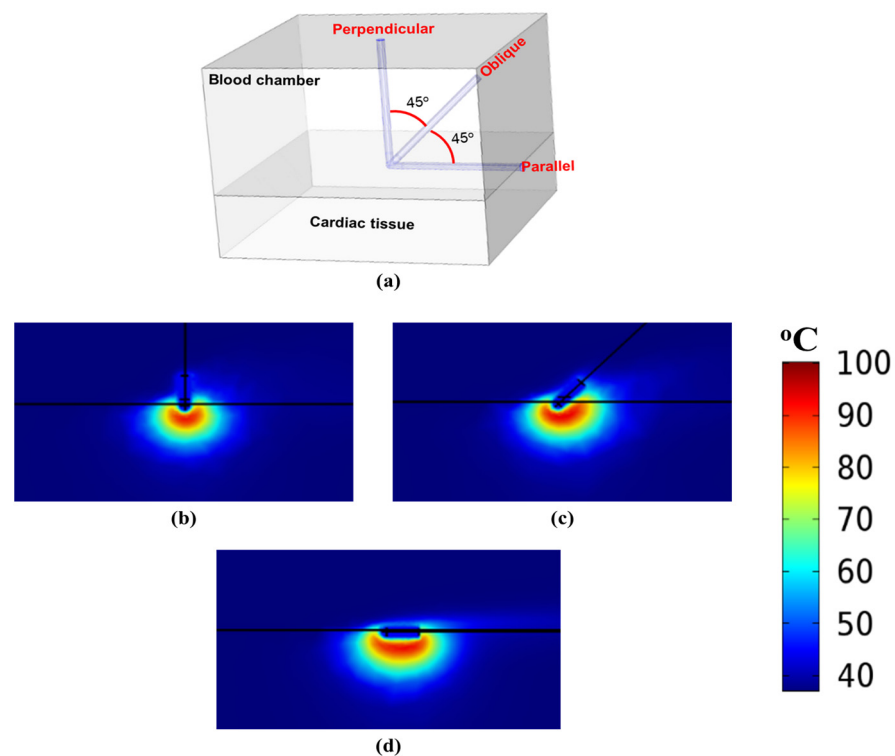
Figure 6. (**a**) Schematic of three different orientations of the RF electrode with respect to cardiac tissue. Temperature distribution obtained after 60 s of cardiac ablation with: (**b**) perpendicular (90°), (**c**) oblique (45°), and (**d**) parallel (0°) orientations of the electrode.
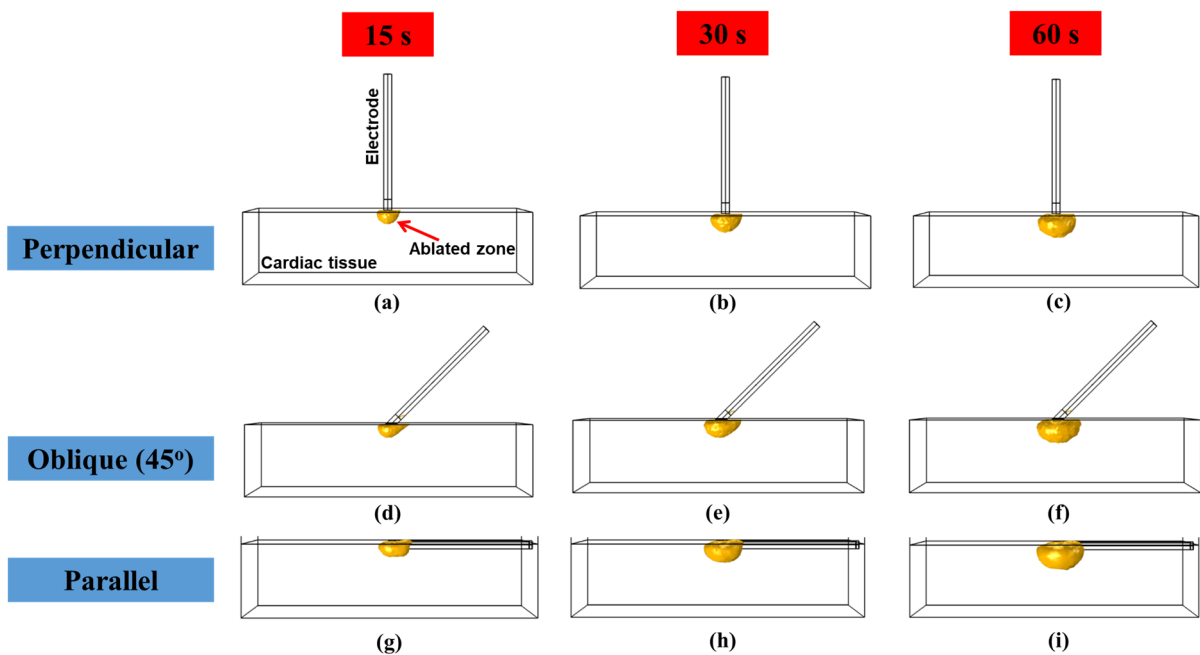
Figure 7. Propagation of ablation zone during 60 s of cardiac ablative procedure for: (**a–c**) perpendicular (90°), (**d–f**) oblique (45°), and (**g–i**) parallel (0°) configuration of electrode.
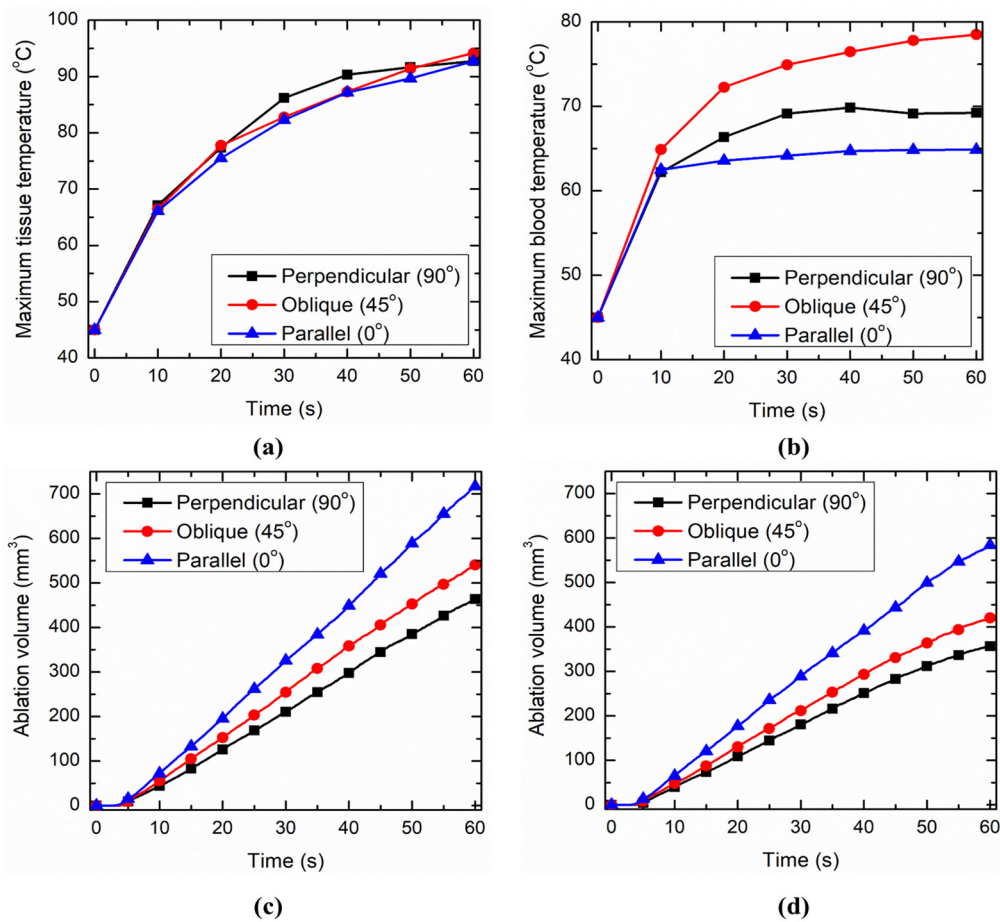
Figure 8. Temporal variation of: (**a**) maximum tissue temperature, and (**b**) maximum blood temperature for different orientations of electrodes. Comparison of ablation volumes predicted with different orientations of the electrodes for: (**c**) low blood flow rate, and (**d**) high blood flow rate conditions.

4. Conclusions

In this contribution, a fully coupled electro-thermo-mechanical model has been developed incorporating fluid–structure interactions, non-Fourier effects and a porous media framework, for providing more accurate, precise and realistic estimates of the temperature distribution and ablation volumes attained during the cardiac ablation procedures. Parametric studies have been conducted to quantify the effect of different factors, viz., porosity, thermal relaxation times, blood flow rates, electrode insertion depths and electrode orientations. The presented results would assist the clinicians in the treatment planning stage of the therapies by providing key quantitative information about the effect of critical factors on the efficacy of the cardiac ablation. Further development of the presented results is anticipated along with exploration of the additional coupled effects between the physical fields involved, tissue-cellular scale interactions, and integration of clinical data via efficient data-driven algorithms, including those derived within a machine learning framework. It is expected that the developed model and its further extensions would contribute to the goal of advancing patient-specific models of cardiac ablation that can be readily integrated to hospital work-flow.

References

1. Almekkawy, M.; Chen, J.; Ellis, M.D.; Haemmerich, D.; Holmes III, D.R.; Linte, C.A.; Panescu, D.; Pearce, J.; Prakash, P.; Zderic, V. Therapeutic systems and technologies: State-of-the-art applications, opportunities, and challenges. *IEEE Rev. Biomed. Eng.* **2019**, *13*, 325–339. [CrossRef]
2. Kok, H.P.; Cressman, E.N.; Ceelen, W.; Brace, C.L.; Ivkov, R.; Grüll, H.; Ter Haar, G.; Wust, P.; Crezee, J. Heating technology for malignant tumors: A review. *Int. J. Hypeth.* **2020**, *37*, 711–741. [CrossRef] [PubMed]
3. Chu, K.F.; Dupuy, D.E. Thermal ablation of tumours: Biological mechanisms and advances in therapy. *Nat. Rev. Cancer* **2014**, *14*, 199–208. [CrossRef] [PubMed]
4. Singh, S.; Melnik, R. Thermal ablation of biological tissues in disease treatment: A review of computational models and future directions. *Electr. Biol. Med.* **2020**, *39*, 49–88. [CrossRef]
5. Huang, S.K.S.; Miller, J.M. *Catheter Ablation of Cardiac Arrhythmias*; Elsevier: Philadelphia, PA, USA, 2020.
6. González-Suárez, A.; Berjano, E. Comparative analysis of different methods of modeling the thermal effect of circulating blood flow during RF cardiac ablation. *IEEE Trans. Biomed. Eng.* **2015**, *63*, 250–259. [CrossRef] [PubMed]
7. González-Suárez, A.; Berjano, E.; Guerra, J.M.; Gerardo-Giorda, L. Computational modeling of open-irrigated electrodes for radiofrequency cardiac ablation including blood motion-saline flow interaction. *PLoS ONE* **2016**, *11*, e0150356. [CrossRef]
8. González-Suárez, A.; Pérez, J.J.; Berjano, E. Should fluid dynamics be included in computer models of RF cardiac ablation by irrigated-tip electrodes? *Biomed. Eng. Online* **2018**, *17*, 1–14. [CrossRef] [PubMed]
9. Linte, C.A.; Camp, J.J.; Rettmann, M.E.; Haemmerich, D.; Aktas, M.K.; Huang, D.T.; Packer, D.L.; Holmes III, D.R. Lesion modeling, characterization, and visualization for image-guided cardiac ablation therapy monitoring. *J. Med. Imaging* **2018**, *5*, 021218. [CrossRef]

10. Pérez, J.J.; González-Suárez, A.; Berjano, E. Numerical analysis of thermal impact of intramyocardial capillary blood flow during radiofrequency cardiac ablation. *Int. J. Hypeth.* **2018**, *34*, 243–249. [CrossRef]
11. Tucci, C.; Trujillo, M.; Berjano, E.; Iasiello, M.; Andreozzi, A.; Vanoli, G.P. Pennes' bioheat equation vs. porous media approach in computer modeling of radiofrequency tumor ablation. *Sci. Rep.* **2021**, *11*, 5272. [CrossRef]
12. Andreozzi, A.; Brunese, L.; Iasiello, M.; Tucci, C.; Vanoli, G.P. Modeling heat transfer in tumors: A review of thermal therapies. *Ann. Biomed. Eng.* **2019**, *47*, 676–693. [CrossRef]
13. Petras, A.; Leoni, M.; Guerra, J.M.; Jansson, J.; Gerardo-Giorda, L. A computational model of open-irrigated radiofrequency catheter ablation accounting for mechanical properties of the cardiac tissue. *Int. J. Numer. Methods Biomed. Eng.* **2019**, *35*, e3232. [CrossRef] [PubMed]
14. Singh, S.; Melnik, R. Computational modeling of cardiac ablation incorporating electrothermomechanical interactions. *J. Eng. Sci. Med. Diagn. Ther.* **2020**, *3*, 041004. [CrossRef]
15. Yan, S.; Gu, K.; Wu, X.; Wang, W. Computer simulation study on the effect of electrode–tissue contact force on thermal lesion size in cardiac radiofrequency ablation. *Int. J. Hypeth.* **2020**, *37*, 37–48. [CrossRef] [PubMed]
16. Singh, S.; Melnik, R. Computational model of radiofrequency ablation of cardiac tissues incorporating thermo-electro-mechanical interactions. In Proceedings of the ASME International Mechanical Engineering Congress and Exposition, Virtual Conference, Online, 16–19 November 2020; Volume 84522. [CrossRef]
17. Irastorza, R.M.; Gonzalez-Suarez, A.; Pérez, J.J.; Berjano, E. Differences in applied electrical power between full thorax models and limited-domain models for RF cardiac ablation. *Int. J. Hypeth.* **2020**, *37*, 677–687. [CrossRef] [PubMed]
18. Nguyen, D.M.; Qian, P.; Barry, T.; McEwan, A. The region-of-interest based measurement selection process for electrical impedance tomography in radiofrequency cardiac ablation with known anatomical information. *Biomed. Signal Process. Control* **2020**, *56*, 101706. [CrossRef]
19. Singh, S.; Melnik, R. Coupled thermo-electro-mechanical models of cardiac ablation at tissue-cellular scales and a role of microtubules. In Proceedings of the 14th World Congress in Computational Mechanics and ECCOMAS Congress (WCCM-ECCOMAS), Virtual Conference, Online, 11–15 January 2021. [CrossRef]
20. Iasiello, M.; Andreozzi, A.; Bianco, N.; Vafai, K. The porous media theory applied to radiofrequency catheter ablation. *Int. J. Numer. Methods Heat Fluid Flow* **2019**, *30*, 2669–2681. [CrossRef]
21. Singh, S.; Melnik, R. Coupled thermo-electro-mechanical models for thermal ablation of biological tissues and heat relaxation time effects. *Phys. Med. Biol.* **2019**, *64*, 245008. [CrossRef]
22. Pérez, J.J.; González-Suárez, A.; Nadal, E.; Berjano, E. Thermal impact of replacing constant voltage by low-frequency sine wave voltage in RF ablation computer modeling. *Comput. Methods Programs Biomed.* **2020**, *195*, 105673. [CrossRef]
23. Keangin, P.; Rattanadecho, P. Analysis of heat transport on local thermal non-equilibrium in porous liver during microwave ablation. *Int. J. Heat Mass Transf.* **2013**, *67*, 46–60. [CrossRef]
24. Zhang, Y. Generalized dual-phase lag bioheat equations based on nonequilibrium heat transfer in living biological tissues. *Int. J. Heat Mass Transf.* **2009**, *52*, 4829–4834. [CrossRef]
25. Li, C.; Chen, S.; Wang, Q.; Li, H.; Xiao, S.; Li, F. Effects of thermal relaxation on temperature elevation in ex vivo tissues during high intensity focused ultrasound. *IEEE Access* **2020**, *8*, 212013–212021. [CrossRef]
26. Strunin, D.V.; Melnik, R.V.N.; Roberts, A.J. Numerical modelling of thermoelastic processes using nonlinear theories with thermal relaxation time. *ANZIAM J.* **2000**, *42*, C1356–C1378. [CrossRef]
27. Strunin, D.V.; Melnik, R.V.N.; Roberts, A.J. Coupled thermomechanical waves in hyperbolic thermoelasticity. *J. Therm. Stress.* **2001**, *24*, 121–140.
28. Melnik, R.V.N.; Strunin, D.V.; Roberts, A.J. Nonlinear analysis of rubber-based polymeric materials with thermal relaxation models. *Numer. Heat Transf. Part A Appl.* **2005**, *47*, 549–569. [CrossRef]
29. Chaichanyut, M.; Tungjitkusolmun, S. Microwave ablation using four-tine antenna: Effects of blood flow velocity, vessel location, and total displacement on porous hepatic cancer tissue. *Comput. Math. Methods Med.* **2016**, *2016*, 4846738. [CrossRef]
30. Bhowmik, A.; Repaka, R.; Mishra, S.C. Thermographic evaluation of early melanoma within the vascularized skin using combined non-Newtonian blood flow and bioheat models. *Comput. Biol. Med.* **2014**, *53*, 206–219. [CrossRef]
31. Mohammadpour, M.; Firoozabadi, B. Numerical study of the effect of vascular bed on heat transfer during high intensity focused ultrasound (HIFU) ablation of the liver tumor. *J. Therm. Biol.* **2019**, *86*, 102431. [CrossRef]
32. Paul, A.; Paul, A. Thermomechanical analysis of a triple layered skin structure in presence of nanoparticle embedding multi-level blood vessels. *Int. J. Heat Mass Transf.* **2020**, *148*, 119076. [CrossRef]
33. Singh, S.; Bhowmik, A.; Repaka, R. Radiofrequency ablation of malignant breast tumor: A numerical study. In Proceedings of the 23rd National Heat and Mass Transfer Conference and 1st International ISHMT-ASTFE Heat and Mass Transfer Conference, Trivandrum, India, 17–20 December 2015; pp. 17–20.
34. Kaur, J.; Melnik, R.; Tiwari, A.K. Forced convection heat transfer study of a blunt-headed cylinder in non-Newtonian power-law fluids. *Int. J. Chem. React. Eng.* **2021**, *19*, 673–688. [CrossRef]
35. Formaggia, L.; Quarteroni, A.; Veneziani, A. *Cardiovascular Mathematics: Modeling and Simulation of the Circulatory System*; Springer: Milan, Italy, 2010; Volume 1.
36. Quarteroni, A.; Veneziani, A.; Vergara, C. Geometric multiscale modeling of the cardiovascular system, between theory and practice. *Comput. Methods Appl. Mech. Eng.* **2016**, *302*, 193–252. [CrossRef]

37. Quarteroni, A.; Manzoni, A.; Vergara, C. *Mathematical Modelling of the Human Cardiovascular System: Data, Numerical Approximation, Clinical Applications*; Cambridge University Press: Cambridge, UK, 2019; Volume 33.
38. Henri, J.P.M.; Ohayon, R. *Fluid Structure Interaction: Applied Numerical Methods*; Wiley: Hoboken, NJ, USA, 1995.
39. Nobile, F. Numerical Approximation of Fluid-structure Interaction Problems with Application to Haemodynamics. Ph.D. Thesis, EPFL Scientific Publications, Lausanne, Switzerland, 2001. [CrossRef]
40. Dowell, E.H.; Hall, K.C. Modeling of fluid-structure interaction. *Annu. Rev. Fluid Mech.* **2001**, *33*, 445–490. [CrossRef]
41. Kamath, H.; Willatzen, M.; Melnik, R.V. Vibration of piezoelectric elements surrounded by fluid media. *Ultrasonics* **2006**, *44*, 64–72. [CrossRef] [PubMed]
42. Hou, G.; Wang, J.; Layton, A. Numerical methods for fluid-structure interaction—A review. *Commun. Comput. Phys.* **2012**, *12*, 337–377. [CrossRef]
43. Yu, Y. Numerical Methods for Fluid-Structure Interaction: Analysis and Simulations. Ph.D. Thesis, Brown University, Providence, RI, USA, 2014.
44. Liang, F.; Yang, X.; Zhang, W.; Qian, Y.; Melnik, R. Parametric vibration analysis of pipes conveying fluid by nonlinear normal modes and a numerical iterative approach. *Adv. Appl. Math. Mech.* **2019**, *11*, 38–52. [CrossRef]
45. Griffith, B.E.; Patankar, N.A. Immersed methods for fluid–structure interaction. *Annu. Rev. Fluid Mech.* **2020**, *52*, 421–448. [CrossRef]
46. Toma, M.; Chan-Akeley, R.; Arias, J.; Kurgansky, G.D.; Mao, W. Fluid–structure interaction analyses of biological systems using smoothed-particle hydrodynamics. *Biology* **2021**, *10*, 185. [CrossRef] [PubMed]
47. COMSOL. *COMSOL Multiphysics v. 5.5*; COMSOL AB: Stockholm, Sweden, 2019.
48. Andreozzi, A.; Brunese, L.; Iasiello, M.; Tucci, C.; Vanoli, G.P. Numerical analysis of the pulsating heat source effects in a tumor tissue. *Comput. Methods Programs Biomed.* **2021**, *200*, 105887. [CrossRef]
49. Singh, S.; Melnik, R. Domain heterogeneity in radiofrequency therapies for pain relief: A computational study with coupled models. *Bioengineering* **2020**, *7*, 35. [CrossRef]
50. Singh, S.; Melnik, R. Radiofrequency ablation for treating chronic pain of bones: Effects of nerve locations. In Proceedings of the International Work-Conference on Bioinformatics and Biomedical Engineering, Granada, Spain, 8–10 May 2019; Springer: Cham, Switzerland, 2019; pp. 418–429.
51. Singh, S.; Melnik, R. Computational analysis of pulsed radiofrequency ablation in treating chronic pain. In *International Conference on Computational Science*; Springer: Cham, Switzerland, 2019; pp. 436–450.
52. Singh, S.; Repaka, R. Quantification of thermal injury to the healthy tissue due to imperfect electrode placements during radiofrequency ablation of breast tumor. *J. Eng. Sci. Med. Diagn. Ther.* **2018**, *1*, 011002. [CrossRef]
53. Ma, J.; Sun, Y.; Yang, J. Analytical solution of dual-phase-lag heat conduction in a finite medium subjected to a moving heat source. *Int. J. Therm. Sci.* **2018**, *125*, 34–43. [CrossRef]
54. Ma, J.; Yang, X.; Sun, Y.; Yang, J. Thermal damage in three-dimensional vivo bio-tissues induced by moving heat sources in laser therapy. *Sci. Rep.* **2019**, *9*, 1–13.
55. Calzolari, V.; De Mattia, L.; Basso, F.; Crosato, M.; Scalon, A.; Squasi, P.A.M.; Del Favero, S.; Cernetti, C. Ablation catheter orientation: In vitro effects on lesion size and in vivo analysis during PVI for atrial fibrillation. *Pacing Clin. Electrophysiol.* **2020**, *43*, 1554–1563. [CrossRef] [PubMed]